Defective CAPSL function causes impaired retinal angiogenesis through the MYC axis and is associated with familial exudative vitreoretinopathy

Wenjing Liu[1,2,4#], Shujin Li[1,2#], Mu Yang[1,2#], Jie Ma[1#], Lu Liu[1], Ping Fei[3], Qianchun Xiang[1], Lulin Huang[1], Peiquan Zhao[3]*, Zhenglin Yang[1,2]*, Xianjun Zhu[1,2,4]*

[1]The Sichuan Provincial Key Laboratory for Human Disease Gene Study, Center for Medical Genetics, Sichuan Provincial People's Hospital, University of Electronic Science and Technology of China, Chengdu, Sichuan, 610072, China;

[2]Center for Natural Products Research, Chengdu Institute of Biology, Chinese Academy of Sciences;

[3]Department of Ophthalmology, Xinhua Hospital Affiliated to Shanghai Jiao Tong University School of Medicine, Shanghai, China;

[4]Research Unit for Blindness Prevention of Chinese Academy of Medical Sciences (2019RU026), Sichuan Academy of Medical Sciences and Sichuan Provincial People's Hospital, Chengdu, Sichuan, 610072 China.

# Wenjing Liu, Shujin Li, Mu Yang and Jie Ma contributed equally to this work and shoule be recognized as co-first authors.

*Correspondence: Drs. Peiquan Zhao (zhaopeiquan@xinhuamed.com.cn) or Zhenglin Yang (yangzhenglin@cashq.ac.cn) or Xianjun Zhu (xjzhu@uestc.edu.cn).

Abstract

Familial exudative vitreoretinopathy (FEVR) is a severe genetic disorder characterized by incomplete vascularization of the peripheral retina and associated symptoms that can lead to vision loss. However, the underlying genetic causes of approximately 50% of FEVR cases remain unknown. Here, we report two heterozygous variants, c.88C > T (p.Arg30Ter) and c.247C > T (p.Leu83Phe), in calcyphosine like (*CAPSL*), from four patients in two unrelated FEVR-affected families. Both variants exhibited compromised CAPSL protein expression. Vascular

endothelial cell-specific inactivation of *Capsl* in postnatal mice resulted in defective sprouting, delayed radial/vertical vascular progression, compromised endothelial proliferation, and impaired cell migration, recapitulating the human FEVR phenotypes. *CAPSL*-depleted human retinal microvascular endothelial cells (HRECs) exhibited impaired tube formation, decreased cell proliferation, disrupted cell polarity establishment and filopodia/lamellipodia formation, as well as disrupted collective cell migration *in vitro*. Transcriptomic and proteomic profiling of *CAPSL*-depleted HRECs revealed that *CAPSL* abolition inhibited the MYC signaling axis, in which the expression of core MYC targeted genes were profoundly decreased. Furthermore, a combined analysis of *CAPSL*-depleted HRECs and *c-MYC*-depleted human umbilical vein endothelial cells (HUVECs) uncovered similar transcription patterns. Collectively, this study reports a novel FEVR-associated candidate gene, *CAPSL*, which provides valuable information for genetic counseling and prenatal diagnosis of FEVR. This study also reveals that compromised CAPSL function may causes FEVR through MYC axis, shedding light on the potential involvement of MYC signaling in the pathogenesis of FEVR.

Introduction

A well-organized vascular system is crucial for the proper development of most tissue and organ morphogenesis[1,2]. Consequently, angiogenic defects have been associated with several congenital human diseases[3,4]. Familial exudative vitreoretinopathy (FEVR) is a heritable vitreoretinopathy characterized by defective retinal angiogenesis and various complications, such as extensive neovascularization, exudation, retinal folds and detachments, and vision loss[5]. Based on an ocular screening of over sixty thousand Chinese newborns, the estimated prevalence of FEVR is around 0.46%[6]. Due to the significant genetic heterogeneity, FEVR displays all Mendelian forms of inheritance: autosomal dominant (AD), autosomal recessive (AR), or X-linked recessive (XR)[7-9]. To date, mutations in 17 genes and 1 locus have been identified to cause FEVR, including Norrin (*NDP*)[10], frizzled 4 (*FZD4*)[11], low-density lipoprotein receptor related protein 5 (*LRP5*)[12,13], low-density lipoprotein receptor-related protein 6 (*LRP6*)[14], tetraspanin-12 (*TSPAN12*)[15,16], α-catenin (*CTNNA1*)[17], β-catenin (*CTNNB1*)[18-20], p120-catenin (*CTNND1*)[21], zinc finger protein 408 (*ZNF408*)[22], kinesin family member 11 (*KIF11*)[23], atonal homolog 7 (*ATOH7*)[24], exudative vitreoretinopathy 3 (*EVR3*)[25], integrin-linked kinase (*ILK*)[26], jagged canonical Notch ligand 1 (*JAG1*)[27], discs large MAGUK scaffold protein 1 (*DLG1*)[28], transforming growth factor beta receptor 2 (*TGFBR2*)[29], sorting nexin 31 (*SNX31*)[30], and ER membrane protein complex subunit 1 (*EMC1*)[31]. Nevertheless, these mutations can explain only approximately 50% of FEVR cases[32,33].

Calcyphosine like (*CAPSL*) is a protein-coding gene whose function remains elusive. In 2019, Julia Schreml pointed out that *CAPSL* is a promising candidate gene for multiple symmetric lipomatosis (MSL), a rare adipose tissue disorder of largely unknown etiology[34]. Nevertheless, the specific pathogenic mechanism by which CAPSL triggers MSL remains unclear. The molecular mechanisms governing cellular processes and signaling cascades regulated by CAPSL have yet to be elucidated.

MYC gene family is one of the most widely investigated cancer-causing genes, being implicated in the formation, maintenance, and progression of several different

cancer types, such as breast cancer, lymphoma, and prostatic cancer[35-38]. *c-MYC* is a master regulator in MYC signaling, which participates in cell metabolism, proliferation, differentiation, and migration[39]. The important role of *c-Myc* in vascularization and angiogenesis during tumor development has already been reported in mouse models[40,41]. Vascular endothelial cell (EC)-specific knockout of *c-Myc* in mice leads to impaired vascular expansion, thinned and poorly branched vascular, and reduced endothelial proliferation[42]. Conversely, EC-specific *c-Myc* over-expression caused sustained vascular outgrowth, increased endothelial cell proliferation, and vessel density[42]. These studies indicate that c-MYC is a regulating factor in coordinating endothelial cell behavior and vessel development.

In the current study, from a large cohort of FEVR patients, we identified a missense mutation and a stop-gain mutation in the *CAPSL* gene from four FEVR patients by whole exome sequencing (WES) analysis. Furthermore, endothelial cell (EC)-specific *Capsl* knockout mouse model exhibited FEVR-like retinal vascular defects, emphasizing the indispensable role of *Capsl* for the retinal vascular architecture. Knockdown of *CAPSL* led to compromised proliferation of stalk ECs and retarded migration of tip ECs by regulating the MYC signaling axis. Collectively, this study not only identifies *CAPSL* as a candidate gene for FEVR, but also presents that a compromised MYC signaling axis might contribute to FEVR.

Results

WES analysis revealed two *CAPSL* variants in FEVR patients

To evaluate the causative variants that account for FEVR, we applied WES on genomic DNA samples from 120 FEVR families without mutations in known FEVR genes. Sanger sequencing was further applied to validate the variants and genotype-phenotype co-segregation analysis. Thus, two novel candidate variants in the *CAPSL* gene (NM_144647) were identified in patients with FEVR, and the variants were predicted to be pathogenic by Mutation taster, Polyphen-2, and PROVEAN (Table S1). In family 3036, a heterozygous c.88C>T (p.R30X) variant was identified in an infant (age 0-5 years old) (Figure 1A). His father was a

heterozygous carrier and manifested vascular defects in the retina, including peripheral neovascularization area and leakage by fundus fluorescein angiography, whereas the wild-type mother showed normal vision (Figures 1B and D). The affected amino acid is highly conserved among different species (Figure 1C). The proband (II:1) in the 3104 family has been diagnosed with FEVR and identified with a heterozygous variant c.247C>T (p.L83F) (Figure 1A). His father has also been identified as a carrier of this heterozygous variant, manifested with FEVR symptoms, according to the medical records. Nevertheless, clinical examination data are presently unavailable.

To determine the pathogenesis of *CAPSL* variants for FEVR, we first investigated the effect of variants on the expression of *CAPSL*. Wild-type and mutant coding sequences of *CAPSL* were introduced to the GFP-tagged pcDNA3.1 vector, and an IRES2 box was inserted to prevent the fusion expression of CAPSL and GFP. Immunoblot analysis of cells transfected with plasmids revealed that the CAPSL-R30X protein was undetectable, and the L83F variant resulted in a considerably reduced protein level (Fig.1E and F). Conversely, neither variant influenced the mRNA levels of *CAPSL* (Fig.1G). CAPSL is localized in both the cytoplasm and the nucleus of cells (https://www.proteinatlas.org/), and we then further verified whether these variants have any impact on CAPSL localization. Immunocytochemistry analysis revealed that, consistent with immunoblot analysis, CAPSL-R30X protein was undetectable, and CAPSL-L83F mutant protein exhibited no significant change in localization (Fig.S1). The TGA stop codon can also have an effect on alternative splicing in certain scenarios, and bioinformatics predictions suggested that the impact of *CAPSL* 88C>T variant on alternative splicing is minimal (Fig.S2).Thus, these variants may cause FEVR by reducing CAPSL protein abundance.

Depletion of *Capsl* in vascular endothelial cells caused FEVR-liked phenotypes

We generated an inducible endothelial (EC)-specific *Capsl*-knockout mouse model by breeding mice carrying a loxp-flanked allele of *Capsl* with

tamoxifen-inducible *Pdgfb-iCreER*[43] transgenic animals to determine whether depletion of *Capsl* in mouse endothelial cells could cause FEVR-like phenotypes (Fig.S3A). *Capsl*$^{loxp/loxp}$, *Pdgfb-CreER* mice (hereafter named *Capsl*$^{iECKO/iECKO}$), *Capsl*$^{loxp/+}$, *Pdgfb-CreER* mice (hereafter named *Capsl*$^{iECKO/+}$), and their control littermates (*Capsl*$^{loxp/loxp}$ and *Pdgfb-CreER*, hereafter named Ctrl) were induced by consecutive intraperitoneal injection of 50 μg tamoxifen per pup at postnatal day 1 (P1) to P3 before sacrifice (Fig.S3B and C). *Capsl*$^{iECKO/iECKO}$ mice showed indistinguishable overall appearance compared to their Ctrl littermates. The efficiency of EC-specific deletion of *Capsl* was confirmed by real-time quantitative PCR (RT-qPCR) and western blot analysis of P35 mouse lung tissues (Fig.S3D). The results showed a pronounced reduction in CAPSL expression, at both mRNA and protein levels, in *Capsl*$^{iECKO/iECKO}$ mice compared to Ctrl littermates.

FEVR is a genetically heterogeneous eye disease characterized by incomplete vascularization of the peripheral retina in human patients. We initially assessed the vascular development in P5 *Capsl*$^{iECKO/+}$ mice. The results indicate that *Capsl*$^{iECKO/+}$ mice show no overt differences in vascular progression, vessel density, and vessel branchpoints compared to littermat Ctrls (Fig.S4). This phenotype resembles that of heterozygous knockout mice of certain FEVR pathogenic gene, such as *Lrp5* heterogeneous knockout mice[44]. To assess the role of *CAPSL* in the growth and patterning of retinal vasculature, we further employed retinal flat-mount analysis to visualize the retinal vessels at different postnatal ages in homozygous mice. As expected, the radial vascular growth, vessel density, and vascular branching are dramatically reduced in P5 *Capsl*$^{iECKO/iECKO}$ retina relative to Ctrl mice (Fig.2A and D-F). The number of retinal vascular tip cells, which leads EC migration toward high VEGFA by extending filopodia at the angiogenic front[45], was considerably decreased and sparsely distributed in *Capsl*$^{iECKO/iECKO}$ retinaes, compared to that of control littermates (Fig.2B-C and G-H).

The onset of mouse retinal vascular development occurs postnatally at P0, coinciding with the regression of the hyaloid vasculature[46,47]. Similar to the previous reported hyaloid phenotypes observed in the FEVR-associated mouse models[15,48],

the hyaloid vasculature in *Capsl*$^{iECKO/iECKO}$ at P10 displayed delayed regression in comparison to the Ctrl littermates (Fig.3A). Following the expansion of the superficial vessel plexus at around P8, retinal vessels extend perpendicularly into the deep retina, forming secondary and deep third capillary layers[49]. To investigate whether the depletion of *Capsl* hinders deep capillary vascular development, we conducted immunostaining on P10 retinal sections. The results revealed a delayed development of deep retinal vessels in *Capsl*$^{iECKO/iECKO}$ mouse retinae compared to that of Ctrl (Fig.3B). In addition, immunostaining of P14 flat-mount retina confirmed an incomplete architecture of the deep vascular layer in *Capsl*$^{iECKO/iECKO}$ mouse (Fig.3C). By P21, EC growth was closely resembling control retinas in *Capsl*$^{iECKO/iECKO}$ mice when angiogenesis almost complete (Fig.S5).

The development of retinal vasculature is a complex process encompassing not only the coordinated behavior of endothelial cells but also the intricate interactions among different cell types and cytokines within the retina[50]. Astrocytes form a mesh as a template prior to vascular growth and guide angiogenic expansion by secreting gradient distributed VEGFA[51-53]. Abnormal activation of astrocytes and subsequent inflammatory responses have been observed in multiple FEVR mouse models[15,17,49,54]. To explore whether the gradient and expression level of VEGFA were affected by the depletion of *Capsl*, we conducted immunostaining of VEGFA on the retina. However, the results showed no alteration of VEGFA (Fig.S6A). Meanwhile, the activation state and the pattern of the vascular template for EC outgrowth formed by astrocytes remained normal, indicated by GFAP (Fig.S6B). Pericyte recruitment is necessary for vessel stability and maturation[55]. The immunostaining of Desmin or NG2 staining exhibited no difference between Ctrl and *Capsl*$^{iECKO/iECKO}$ mice (Fig.S6C). To assess the integrity of the retinal vascular barrier, we performed the intraperitoneal injection of biocytin-TMR (869 Da), a small-molecular-weight fluorescent tracer[56]. The results showed no notable leakage in the *Capsl*$^{iECKO/iECKO}$ retina, suggesting the intact blood barrier despite the depletion of ECs-*Capsl* (Fig.S6D). The extracellular matrix (ECM) coordinates the behavior of ECs by regulating cell-cell communication processes[57]. The deficiency and abnormal

accumulation of ECM can both disrupt the adhesion, proliferation, and migration of the endothelial cells, leading to defects in blood vessel architecture[58-60]. We thus analyzed the extracellular matrix accumulation using fibronectin 1, and the result showed normal deposition of ECM (Fig.S6E). In conclusion, endothelial cell-specific knockout of *Capsl* may mainly lead to defects in retinal vascular ECs rather than other vascular-associated cells.

CAPSL controls vascular proliferation and migration

Considering the compromised vascular progression and decreased vessel density in *Capsl*$^{iECKO/iECKO}$ mouse retinae, we first performed the EdU assay on retina flat-mounts co-stained with ETS transcription factor ERG (endothelial cell nuclear marker) to assess the proliferation of ECs. The results showed a strongly reduced proliferation of *Capsl*-defective ECs compared to that of Ctrl (Fig.4A). As previously reported, the regressed retinal vessels exhibited sleeve-like positivity for basement matrix component Collagen IV and negativity for Isolectin IB4[61]. To compare the vascular regression between *Capsl*$^{iECKO/iECKO}$ and Ctrl retinae, we conducted co-staining of the Collagen IV and IB4. The results revealed that depletion of *Capsl* leads to an increased vascular regression, evidenced by a significant increase in collagen IV basal membrane sleeves lacking IB4 both in the capillary plexus and angiogenic front (Fig.4B).

Additionally, considering the pivotal role of tip cells in the direction of vascular development, we then asked whether depletion of *Capsl* impairs the polarity of tip cells by analyzing the morphology of cell nuclei at the angiogenic front. This analysis was based on the observation that the nuclei of actively migrating tip cells are elliptical and exhibit increased sphericity(decreased ellipticity)in static tip cells[62,63]. In Ctrl mice retinae, the nuclei of tip ECs were predominantly elliptical, pointing towards the avascular area (Fig.4C). Conversely, in the retinae of *Capsl*$^{iECKO/iECKO}$ mice, the nuclei of tip ECs appeared more spherical and did not orient towards the avascular area (Fig.4C). These findings suggest that CAPSL is critical for EC

proliferation, vascular regression, and cell polarity.

Endothelial *CAPSL* is required for cell polarity and filopodia/lamellipodia formation

To investigate the functional mechanism and signaling cascade by which CAPSL regulates EC behaviors, we performed *in vitro* experiments on primary human retinal microvascular endothelial cells (HRECs). Stable *CAPSL* knockdown HRECs were generated using the lentivirus-mediated shRNA system. RT-qPCR analysis showed that the mRNA level of *CAPSL* was significantly decreased (Fig.S1E). In line with the overall reduced vascular coverage in *Capsl*$^{iECKO/iECKO}$ mice retina, *CAPSL*-knockdown HRECs (sh*CAPSL*-ECs) exhibited considerably impaired tube formation *in vitro* (Fig.5A). EdU labeling also revealed decreased cell proliferation of sh*CAPSL*-ECs compared to that of shCtrl-ECs (Fig.5B). We further conducted flow cytometry to determine whether cell cycle arrest occurred upon depletion of *CAPSL* in HRECs. The redistribution of cell cycle phases indicated that the cell cycle was arrested during the G0/G1 phase in the sh*CAPSL*-ECs (Fig.5C-D). To further investigate the role of CAPSL in EC migration, we performed the scratch-wound assay in confluent sh*CAPSL*-ECs and shCtrl-ECs, as previously reported[63,64]. Nine hours after scratching, ECs were co-stained with GM130 and phalloidin to visualize the Golgi apparatus and the cytoskeleton. The results indicated that the nuclei of sh*CAPSL*-ECs were more spherical than those of shCtrl-ECs (Fig.5E-F). Given that the axial polarity can reflect the direction and migration of ECs[65,66], we further measured the cell polarity (nucleus-to-Golgi polarity axis) of ECs at the wound edge[63,64]. As a result, the Golgi apparatus of shCtrl-ECs was predominantly positioned around the wound edge, while that of sh*CAPSL*-ECs showed more random positioning[67] (Fig.5H).

At the angiogenic front, the dynamic behaviors of tip cells largely rely on the rearrangement and organization of the actin cytoskeleton[68]. Tip cells extend actin-driven filopodia and lamellipodia to probe chemotactic guidance cues, providing direction and migration for the developing vascular network[69-71]. Notably, sh*CAPSL*-ECs exhibited fewer filopodia, smaller lamellipodia, and significantly

impaired wound closure compared to shCtrl-ECs at the wound scratch edge (Fig.5I). Also, as expected, sh*CAPSL*-ECs exhibited significantly impaired wound closure at the same time point after scratching relative to shCtrl-ECs (Fig.5J). Small Rho GTPases, including CDC42 and Rac, are essential for lamellipodial extension and cell migration[72,73]. Western blot analysis uncovered markedly attenuated expression of CDC42, RHOA, and Rac1 (Fig.5K). Moreover, both MYL9 and phosphorylated MYL9 at Ser19, which are crucial regulators of contractile force, were also drastically reduced in sh*CAPSL*-ECs compared to those of shCtrl-ECs (Fig.5K). These results indicated that CAPSL regulates EC polarity, filipodia/lamellipodia formation, and migration by modulating the actomyosin cytoskeleton.

CAPSL regulates endothelial cell proliferation through the MYC signaling axis

Given the fact that FEVR is predominantly characterized by the compromised Norrin/β-catenin signaling pathway as its main causative factor[10,15,17,18], we first asked whether loss of CAPSL function causes FEVR through Norrin/β-catenin signaling. TopFlash reporter gene system was used to determine the activity of the Norrin/β-catenin signaling pathway. Knocking down *CAPSL* expression in human embryonic kidney 293 (HEK293) SuperTopFlash (STF) cells led to similar luciferase activity, compared to cells transfected with shCtrl (Fig.S7A). Furthermore, transfection of *shRNA*-resistant CAPSL plasmid (WT, R30X, or L83F) in *CAPSL*-knockdown 293STF cells resulted in no significant difference in luciferase activity (Fig.S7B). These results indicated that *CAPSL* was not a major player in Norrin/β-catenin signaling to regulate retinal vascular development.

We next performed unbiased transcriptomic and proteomic analyses on the control and *CAPSL*-knockdown HRECs to explore the underlying mechanism by which *CAPSL* regulates EC proliferation and migration. RNA sequencing (RNA-seq) identified 1961 up-regulated genes and 2205 down-regulated genes in sh*CAPSL*-ECs compared to shCtrl-ECs (logFC>0.58, Pvalue<0.05), 1342 up-regulated genes and 1218 down-regulated genes in ECs overexpressing CAPSL (LentiOE-ECs) compared to Ctrl-ECs (Fig.6A). Gene set enrichment analysis (GSEA) on transcriptomic data

showed multiple down-regulated signaling axes upon the depletion of *CAPSL*, including E2F targets (NES=-3.2944438, P value=0), G2/M checkpoints（NES=-3.2851038, Pvalue=0）, MYC targets（NES=-2.8795638, P value=0）, and mitotic spindle (NES=-2.646523, Pvalue=0) (Fig.6B-C). In line with this, overexpression of CAPSL in HRECs also caused a significant increase in E2F targets (NES=2.7765026, P value=0), G2/M checkpoints (NES=2.6528199, Pvalue=0), and MYC targets (NES=2.6528199, Pvalue=0) (Fig.6D-E). Meanwhile, proteomic profiling showed similar expression patterns with that of transcriptomic profiling upon knockdown or overexpression of *CAPSL* (Fig.6F-I). Furthermore, we applied correlation analysis on the transcriptomic and proteomic data, which divided the genes into 9 quadrants (Fig. 6J). GSEA analysis was performed on genes in the third and seventh quadrants, which were regulated at the transcriptional level (Fig. 6K and Dataset S1). Interestingly, the down-regulated signaling pathways are highly consistent with those observed in GSEA analysis of both transcriptomic and proteomic analyses (Fig.6K). Given that the c-MYC was an established driver of cell growth and migration[74], and that the genes in the MYC signaling were down-regulated upon *CAPSL*-depletion (Fig.6L), we speculated that CAPSL might play a pivotal role in MYC signaling in HRECs. RT-qPCR analysis was further performed to validate the downregulation fo MYC target genes in the lung tissue of Ctrl and $Capsl^{iECKO/iECKO}$ mice (Fig.S8).

We next incorporated an analysis of transcriptome profiling of human umbilical vein endothelial cells (HUVECs) infected with lentiviruses encoding control- or *c-MYC*-targeting gRNAs (GSE161815)[75]. Intriguingly, GSEA analysis revealed that ablation of cMYC in HUVECs led to compromised E2F targets, MYC targets, and G2/M checkpoint signaling activity (Fig.7A-B), largely consistent with those observed in the absence of *CAPSL*. This also suggests that cMYC might play a role in the upstream regulation of E2F targets and G2/M checkpoint signaling. Venn diagram analysis of down-regulated genes (LogFC<-0.585, P<0.05) in *CAPSL*-depleted HRECs and *c-MYC*-depleted HUVECs revealed a large proportion of shared genes,

indicative of similar transcriptional regulatory patterns between CAPSL and cMYC (Fig.7C and Dataset S2). Additionally, these genes are predominently enriched in the MYC targets signaling (Fig.7D-F).

We, therefore, asked whether CAPSL regulates c-MYC expression. Notably, the depletion of *CAPSL* significantly decreased the protein level of c-MYC, rather than the mRNA level in HRECs (Fig.7G). Subsequently, western blot analysis revealed that expression levels of c-MYC target genes, such as MCM family, E2F1, CyclinD family, and PCNA, were decreased in the absence of *CAPSL* in HRECs (Fig.7H-I). Taken together, these findings suggest c-MYC as a potential functional regulator downstream of CAPSL.

Discussion

Over the last decades, major progress has been made in understanding the molecular mechanisms underlying FEVR, and 17 FEVR-causing genes have been identified[10-31]. However, the pathogenic genes and mechanisms underlying approximately 50% of clinical cases remain elusive[20,21]. In this study, we report a new FEVR candidate gene *CAPSL* and uncover the pivotal roles of CAPSL in retina vascular development. The EC-specific *Capsl*-knockout mouse model exhibited FEVR phenotypes, including delayed vascular progression, retarded hyaloid vessel regression, and decreased vessel density. Deficiency of CAPSL in ECs resulted in compromised cell proliferation and defective EC migration, providing insights into the regulatory roles of CAPSL in retina vascularization (Fig.2-5).

During retinal development, angiogenesis comprises various processes such as endothelial cell (EC) specification, adhesion, proliferation, migration, and pruning[49]. The regulation of angiogenesis entails the control of EC behaviors and the interactions between ECs, extracellular matrix (ECM), and other types of retinal cells[65]. In this study, we observed impaired radial expansion and vertical invasion, as well as the increased pruning of the retinal vascular ECs upon inactivating endothelial *Capsl* (Fig.2-3). However, neither the expression level nor the gradience of VEGFA was disturbed in $Capsl^{iECKO/iECKO}$ mice, which could be attributed to the intact blood

barrier in the *Capsl*$^{iECKO/iECKO}$ retina (Fig.S6). In addition, the loss of *Capsl* resulted in the presence of more spherical tip cell nuclei, which were directed more randomly to the avascular area (Fig.4). These results provide evidence that CAPSL acts as a novel regulator for collective EC behavior.

In vitro functional studies demonstrated that depletion of *CAPSL* impaired tube formation, EC proliferation ability, and EC polarity (Fig.5). Moreover, the formation of filopodia and lamellipodia is also disturbed by the depletion of *CAPSL* (Fig.5). Using the unbiased transcriptomic and proteomic sequencing, bioinformatic analysis, and western blot assay, we demonstrated that the defects in *CAPSL* affect EC function by down-regulating the MYC signaling cascade (Fig.6-7). c-MYC has been shown to be a critical mediator of anabolic metabolism, cell growth, and migration[76,77]. Aberrant upregulation of the MYC signaling pathway is frequently observed in many types of cancers[78,79]. Interestingly, the phenotypes of retinal vessels in *Capsl*$^{iECKO/iECKO}$ mice resemble the vascular defects in *c-Myc*$^{iECKO/iECKO}$ mice, exhibiting FEVR-like phenotypes, such as impaired vascular progression, decreased branch points, and reduced EC proliferation[39,42].

The Norrin/β-catenin signaling pathway is a subset of Wnt signaling pathway that is specifically activated during vascular development of the central nervous system[20,80]. Although several signaling pathways have been implicated in the pathogenesis of FEVR, variants in crucial components of Norrin/β-catenin signaling account for most of the FEVR cases[15,17,18]. It is worth mentioning that c-MYC is widely recognized as a downstream target of Wnt signaling, which is transcriptionally regulated during Wnt activation[81-83]. However, to our knowledge, there is a lack of literature reporting on the correlation between the MYC signaling pathway and FEVR. Interestingly, here we proved that the absence of CAPSL leads to a decrease in c-MYC protein level, which down-regulates MYC signaling without affecting Norrin/β-catenin signaling (Fig.7 and S7). Consequently, we propose c-MYC as a potential therapeutic target for FEVR, a hypothesis that warrants substantiation through subsequent investigations.

Additionally, the formation of filopodia and lamellipodia, which is reported to be

intimately related to the actomyosin dynamics and the activity of small Rho GTPases such as CDC42[84,85], is significantly reduced in *CAPSL*-defective HRECs. In our study, we confirmed that the knockdown of *CAPSL* led to a significant reduction of CDC42, which might be the causative mechanism behind the disturbed formation of filopodia and lamellipodia (Fig.5).

Taken together, our study demonstrated that *CAPSL* is potentially a novel candidate gene associated with FEVR. We also demonstrated that variants in the *CAPSL* gene, independently of canonical Norrin/β-catenin signaling, cause FEVR through inactivating MYC signaling, expanding FEVR-involved signaling pathways.

Methods

DNA sequencing of patients and controls

The study was approved by the Institutional Research Committees of Sichuan Provincial People's Hospital and Xinhua Hospital Affiliated to Shanghai Jiao Tong University School of Medicine. Informed consent was obtained from all participants and from guardians of minors involved in genetic testing. The patients were clinically diagnosed with exudative vitreoretinopathy. Genomic DNA was extracted from the peripheral blood of FEVR families and control individuals using a blood DNA extraction kit (Qiagen, Germantown, Maryland, USA) according to standard protocol. Whole-exome sequencing (WES) was performed on DNA samples to identify candidate pathogenic genes for FEVR as previously described[17]. Family ID numbers 3036 and 3104 are not known to anyone outside the research group.

Mouse model and genotyping

Capsl$^{loxp/+}$ model was generated using the CRISPR/Cas9 nickase technique by Viewsolid Biotechology (Beijing, China) in C57BL/6J background. The genomic RNA (gRNA) sequence was as follows: Capsl-L gRNA: 5'-CTATCCCAA TTGTGCTCCTGG-3'; Capsl-R gRNA: 5'-TGGGACTCATGGTTCTAGAGG-3'. Pdgfb-iCreER[43] transgenic mice on a mixed background of C57BL/6 and CBA was obtainted from Dr. Marcus Fruttiger and backcrossed to background for 6 generations.

Capsl$^{loxp/+}$ mice were bred with Pdgfb-iCreER[43] transgenic mice to generate *Capsl*$^{loxp/loxp}$, Pdgfb-iCreER mice. Sanger sequencing analysis confirmed that all experimental mice did not harbor confounding mutations such as *rd1* and *rd8* mutations (Fig. S9). Genomic DNA samples extracted from mouse tails were genotyped using PCR to detect loxp-flanked *Capsl* and Pdgfb-iCreER. Primer sets used for *Capsl* loxp were: 5'-GGCAGGTAAGATGGTGTC-3' and 5'-TCTGTTTGTGGATCAATGTG-3'; and primer sets used for Pdgfb-iCreER were: 5'-GCCGCCGGGATCACTCTCG-3' and 5'-CCAGCCGCCGTCGCAACTC-3'. All mice were maintained under specific pathogen-free conditions with standard rodent water and diet, and both males and female mice were used for experimental analysis. Experiments involving animals were conducted in accordance with institutional guidelines and following the protocols approved by the Institutional Animal Care and Use Committee of Sichuan Provincial People's Hospital.

Preparation of flat-mount retinae and retina sections

Enucleated eyes were fixed for 15 min in 4% paraformaldehyde (PFA) at room temperature, followed by immersion in PBS for the same duration. The retinae were then dissected and partially cut into four quadrants as previously described[86]. The dissected retinal cups were post-fixed overnight and then stained as described below. As for retina sections, after fixation in 4% PFA for 2h, the enucleated eyes were dehydrated until they settled to the bottom of the tube with 30% sucrose and then embedded in Tissue Freezing Medium (Servicebio). Specimens were sectioned, cleaned, and stained as previously described[87].

Hyaloid vessel preparation

Neonatal eyes were fixed in 4% PFA for 2h before the cornea, lens, and iris were removed. The eye cup was immersed in 5% gelatin at 4 □ overnight. The solidified gelatin was extricated and heat melted on a glass slide, washed with warm water, air-dried, and imaged with DAPI staining.

Immunohistochemistry

All immunostainings of retinae were performed using littermates with similar body size and treated under the same conditions. The flat-mount retina and retina sections were permeabilized and blocked in PBS containing 5% fetal bovine serum and 0.2% Triton X-100 at room temperature for 2h. Next, they were rinsed in PBS and incubated in directly conjugated Isolectin-B4 Alexa 488 or Alexa 594 (1:200; Thermo Fisher, USA) and primary antibodies in a blocking buffer at 4□ overnight. After three washes, the retinae were processed for multiple labeling or flat-mounted onto microscope glass slides with Fluoromount (Sigma-Aldrich, USA).

For in vivo analysis of cell proliferation, each pup was injected intraperitoneally with 200ug EdU 3h before the mice were euthanasia. Retinae were dissected and permeabilized as previously described. EDU-positive labeling was stained and detected by means of a Click-iT EDU Alexa Fluor-647 Imaging Kit (C10640, Thermo Fisher Scientific, USA) according to the manufacturer's instruction. For paracellular BRB integrity analysis, each pup was injected intraperitoneally with 2% fluorescent tracer, 5-(and-6)-tetramethylrhodamine biocytin, Biocytin-TMR (CAT#T12921, Thermo Fisher Scientific, USA) for 24 hours prior to sacrifice, followed by flat-mount preparation, blocking, and staining of Isolectin B4.

Images of stained flat-mounted retinae, retina sections, and HRECs were acquired using Zeiss LSM 800 confocal microscope (Thornwood, NY, USA) and processed with Zeiss processing software, Angio Tool, and Adobe Photoshop. The detailed information about antibodies used for immunofluorescence is listed in Table S2.

Cell lines and primary cell culture

Human retinal microvascular endothelial cells (HRECs) were purchased from Cell System and cultured in EBM™-2 media (CC-3156, Lonza, Switzerland) containing 5% fetal bovine serum, 0.4% hydrocortisone, 4% Hfgf-b, 0.1% VEGF, 0.1% R3-IGF, 0.1% ascorbic acid, 0.1% hEGF 0.1% GA-1000, and 0.1% heparin at 37°C in a 5% CO_2 incubator. HRECs at passages 3-7 were used for experiments.

HEK-293T were obtained from the American Type Culture Collection (ATCC) and cultured in DMEM (SH30023.01, Hycolon, USA) with 10% fetal bovine serum and cells were maintained at 37°C in a 5% CO_2 incubator.

Gene knockdown and overexpression strategies

HRECs were seeded on 6 cm dishes at the day before transfected with lentivirus carrying shRNA for human *CAPSL* (5'-AAGACCTTCGTGAAGTATA-3', Genechem, Shanghai, China) or negative control shRNA (5'-TTCTCCGAACGTGTCACGT-3') according to the protocol of the manufacture. Cells were incubated for at least 72h before used for further experiments.

For overexpression of exogenous protein in HEK-293T cells, cells were transfected with Lipofectamine-3000 (Invitrogen, USA) according to the manufacturer's instructions.

Matrigel EC tube formation assay

HRECs transfected with the corresponding shRNA after 72h were counted and planted onto the matrigel as previously described[88]. After 6h of incubation at 37□ in a 5% CO_2 incubator, the images were captured under an anatomical lens (Carl Zeiss, Germany).

Immunofluorescence of HREC

After cell counting, the same number of HRECs transfected with shCtrl and shCAPSL were seeded on slides in 24-well plates. Cells were fixed with 4% PFA at room temperature for 15min. After being rinsed in PBS three times, cells were blocked in the blocking buffer at room temperature for 2h. The cells were labeled with primary antibodies overnight at 4□. Following three washes in PBS, Alexa-Fluor-594 or Alexa-Fluor-647 conjugated antibodies were administered along with DAPI, and cells were incubated at room temperature for 1h. After three washes in PBS, stained cells were mounted on microscope glass slides with Fluoromount (Sigma-Aldrich, USA).

For *in vitro* analysis of cell proliferation, 20 μM EdU (Thermo Fisher Scientific, USA) was added into 96-well plated 3h before cells were harvested. EdU-positive cells were stained and detected with the Click-iT EDU Alexa Fluor-647 Imaging Kit (C10640, Thermo Fisher Scientific, USA) according to the manufacturer's instruction.

Wound healing assay

72h after shRNA transfection, HRECs were seeded in 6-well plates with complete medium for 24h until grown to confluence. Plates were then coated with 10 μg/mL fibronectin for half an hour in 37 □ before cell culture. 200 μL pipette tips were used to generate wounds, and each well was washed twice with Utrasalin A (Lonza, Switzerland) to remove detached cells. Cells were then starved in the EBM-2 medium at 37°C in a 5% CO_2 incubator. Images of the wounds were captured with an optical microscope at 0h, 12h, and 16h after the wounds were made, respectively. The wound closure areas were measured using ImageJ software.

For analyses of Golgi apparatus polarization, cells were maintained on 24-well glass slides and fixed with 4% PFA for 15 min at 9 h after cell migration was initiated.

RNA extraction and RT-qPCR

Total RNA was extracted from cultured HRECs or fresh lungs from mouse using TRIzol reagent (Life Technologies, USA) according to the manufacturer's instructions. RNA concentration and quality were measured with NanoDrop 2000 spectrophotometer (Thermo Fisher Scientific, USA), and 1 μg total RNA was reverse transcribed using EasyScript One-Step RT-PCR SuperMix (TransGen Biotech, Beijing, China) following the standard protocol. RT-qPCR was performed using a 7500 Real-Time PCR System (Applied Biosystems, USA) with TransStart Tip Green qPCR Supermix (TransGen Biotech). At least three experiments were performed, and PCR reactions were performed in triplicate. GAPDH was used as a reference gene. The primer sets are listed in Table S3.

Protein extraction and western blotting

HRECs or lung tissue from mice were lysed in standard PIPA lysis buffer (50 mM Tris-HCl, 150 mM NaCl, 1% Triton X-100, 0.5% sodium deoxycholate, 0.1% sodium dodecyl sulfate, pH 7.4) supplemented with Protease and Phosphatase Inhibitor Cocktail (Roche, USA). After sonication, centrifugation, and protein quantification, the supernatant was diluted in 2x SDS loading buffer. Equal amounts of protein (20 μg) were loaded and resolved on 10-15% SDS-polyacrylamide, and Western blotting was performed. After gels were transfected onto a Polubinylidene Difluoride (PVDF) membrane (GE Healthcare, USA), the membranes were incubated in a blocking buffer containing 8% skimmed milk (9999, Cell Signaling Technology) in TBST for 1h at room temperature on a rocking platform, followed by overnight incubation at 4□ with the primary antibodies diluted in blocking buffer. Membranes were then washed in TBST three times and incubated in the blocking buffer containing secondary HRP-conjugated antibodies for 1h at room temperature. Protein blots were visualized with e-BLOT Touch Imager (e-BLOT, China) and blots were relatively quantified with ImageJ. GAPDH was used as an internal reference. Detailed information about antibodies used for western blot is listed in Table S4.

Luciferase Assays

Dual-luciferase assays were performed as previously described[17]. Briefly, 293STF cells were plated on 24-well plates at a confluency of ~30%. The following day, the cells were transfected with corresponding plasmids with lip3000. 48 hours post-transfection, cells were harvested, and the lysates were used to measure Firefly and *Renilla* luciferase activity according to the manufacturer's instructions (TransGen).

Quantification of retinal parameters

All quantifications were done using Zeiss processing software on high-resolution confocal images. Vascular progression was measured in a straight line from the optic nerve to the angiogenic front of the retinal plexus for each retina quadrant (n=6, each group). Vessel density and branch points were calculated with Angio Tool software

from flat-mounted retinae (n=6, each group). Endothelial tip cell numbers were measured by counting endothelial sprouts at the angiogenic front of the entire vascular plexus of the same length (n=6, each group). Endothelial tip cell filopodia density was calculated with high-resolution images (60× objective) of 6 randomly selected angiogenic front fields from 6 retinae per genotype (n=6, each group). Endothelial cell proliferation was calculated by measuring the number of both EDU-positive and ERG-positive cells within retinae of the same size and same position at the edge of the vascular plexus (n=6, each group). Retinal pericyte coverage was quantified by comparing the $NG2^+$ or $Desmin^+$ pericytes with $IB4^+$ vessels (n=6, each group). The nuclear ellipticity of the cells at the scratch edge was calculated by the distance of the nuclear long axis (Height) divided by the maximum vertical distance to the nuclear long axis (Width).

Transcriptomic profiling

Total RNA was extracted from shCtrl-ECs, sh*CAPSL*-ECs, and LentiOE-ECs and quantified using NanoDrop2000 Spectrophotometer (Thermo Fisher Scientific, USA). RNA integrity was determined by Bioanalyzer RNA 6000 Nano assay kit (Agilent, China). RNA library construction was performed with Illumina TruseqTM RNA sample prep Kit and RNA sequencing was performed with Truseq SBS Kit (300 cycles) in BIOZERON (BIOZERON, China). RNA-Seq reads were performed using the TopHat software tool to acquire the alignment file, which was used to quantify mRNA expression and determine the differentially expressed genes. All gene expression values were changed to log2 values for further analysis, and a P value of less than or equal to 0.05 was considered to indicate significance. The gene set enrichment analysis (GSEA) was performed with the omicshare platform (https://www.omicshare.com). The raw data have been uploaded to the Genome Sequence Archive (https://ngdc.cncb.ac.cn/gsa/browse/HRA010305), and the assigned accession number was HRA010305.

Proteomic profiling

Total protein was extracted from shCtrl-ECs, sh*CAPSL*-ECs, and LentiOE-ECs and quantified using a BCA protein quantification kit (Beyotime, China). Samples were sent to PTM Biolab (PTM Biolab, China) to perform proteomic profiling using 4D-Labelfree. All protein expression values were changed to log2 values for further analysis, with a corrected P value< 0.05. The gene set enrichment analysis (GSEA) was performed with the omicshare platform (https://www.omicshare.com). The raw data have been uploaded to the Genome Sequence Archive (https://www.ebi.ac.uk/pride/archive), and the assigned accession number was PXD051696.

Image acquisition and statistical analysis

Immunofluorescence images were obtained using a laser scanning microscope (LSM 900, Zeiss). Statistical analyses were performed with GraphPad Prism 8.0 software. Data were analyzed using the Student's t-test for comparison between two groups or one-way ANOVA followed by Dunnett multiple comparison test for comparison of multiple groups, and plotted as mean ± SD. At least three independent experiments were performed. Image J was used to compare results for the tube formation assay experiments and bands of immunoblot. Results were considered significant when *P **<** 0.05, **P **<** 0.01, ***P **<** 0.001, or ****P **<** 0.0001. “ns” stands for “no significance.”

Study approval

This study was approved by the institutional review board of Sichuan Provincial People’s Hospital (approval number: 2014-009) and Xinhua Hospital Affiliated to Shanghai Jiao Tong University School of Medicine, and informed consent was obtained from all participants or legal guardians for minors. All animal studies were performed according to established ethical guidelines approved by the animal care committee of Sichuan Provincial People’s Hospital.

Data availability

All data produced in the present study are available upon reasonable request to the authors.

Competing interests

All authors declare that there are no competing interests.

Author contributions

XZ, ZY, and PZ conceived the research. WL, SL, MY, and JM performed the animal mouse model research and cell biology, transcriptome, and proteome data analysis. LL, PF, and QX performed animal breeding and genotyping. PZ recruited the participants and performed the WES study. LH performed the Sanger sequencing analysis. WL, SL, MY, and XZ wrote the manuscript, with input from other authors.

Funding

This study was supported by the National Natural Science Foundation of China (82371083, 82121003, 82101153, 82101160), the Department of Science and Technology of Sichuan Province (2023ZYD0172, 2023NSFSC1661, 2023NSFSC0036, and 2022ZYD0059), the CAMS Innovation Fund for Medical Sciences (2019-12M-5-032), Sichuan Intellectual Property Office (China) (No. 2022-ZS-0070), the Fundamental Research Funds for the Central Universities of Ministry of Education of China (ZYGX2022J023), and Sichuan Provincial People's Hospital Postdoctoral fund (2022BH019). The funders had no role in the study design, data collection and analysis, or preparation of the manuscript.

References

[1] Vogenstahl J, Parrilla M, Acker-Palmer A, et al. Vascular Regulation of Developmental Neurogenesis[J]. Front Cell Dev Biol, 2022, 10: 890852.
[2] Ye X, Wang Y, Cahill H, et al. Norrin, frizzled-4, and Lrp5 signaling in endothelial cells controls a genetic program for retinal vascularization[J]. Cell, 2009, 139(2): 285-98.

[3] Carmeliet P, Jain R K. Principles and mechanisms of vessel normalization for cancer and other angiogenic diseases[J]. Nat Rev Drug Discov, 2011, 10(6): 417-27.
[4] Fallah A, Sadeghinia A, Kahroba H, et al. Therapeutic targeting of angiogenesis molecular pathways in angiogenesis-dependent diseases[J]. Biomed Pharmacother, 2019, 110: 775-785.
[5] Yonekawa Y, Thomas B J, Drenser K A, et al. Familial Exudative Vitreoretinopathy: Spectral-Domain Optical Coherence Tomography of the Vitreoretinal Interface, Retina, and Choroid[J]. Ophthalmology, 2015, 122(11): 2270-7.
[6] Fei P, Liu Z, He L, et al. Early detection of ocular abnormalities in a Chinese multicentre neonatal eye screening programme-1-year result[J]. Acta Ophthalmol, 2021, 99(3): e415-e422.
[7] Plager D A, Orgel I K, Ellis F D, et al. X-linked recessive familial exudative vitreoretinopathy[J]. Am J Ophthalmol, 1992, 114(2): 145-8.
[8] Gow J, Oliver G L. Familial exudative vitreoretinopathy. An expanded view[J]. Arch Ophthalmol, 1971, 86(2): 150-5.
[9] De Crecchio G, Simonelli F, Nunziata G, et al. Autosomal recessive familial exudative vitreoretinopathy: evidence for genetic heterogeneity[J]. Clin Genet, 1998, 54(4): 315-20.
[10] Chen Z Y, Battinelli E M, Fielder A, et al. A mutation in the Norrie disease gene (NDP) associated with X-linked familial exudative vitreoretinopathy[J]. Nat Genet, 1993, 5(2): 180-3.
[11] Robitaille J, Macdonald M L, Kaykas A, et al. Mutant frizzled-4 disrupts retinal angiogenesis in familial exudative vitreoretinopathy[J]. Nat Genet, 2002, 32(2): 326-30.
[12] Gong Y, Slee R B, Fukai N, et al. LDL receptor-related protein 5 (LRP5) affects bone accrual and eye development[J]. Cell, 2001, 107(4): 513-23.
[13] Jiao X, Ventruto V, Trese M T, et al. Autosomal recessive familial exudative vitreoretinopathy is associated with mutations in LRP5[J]. Am J Hum Genet, 2004, 75(5): 878-84.
[14] Li S, Yang M, He Y, et al. Variants in the Wnt co-receptor LRP6 are associated with familial exudative vitreoretinopathy[J]. J Genet Genomics, 2022, 49(6): 590-594.
[15] Junge H J, Yang S, Burton J B, et al. TSPAN12 regulates retinal vascular development by promoting Norrin- but not Wnt-induced FZD4/beta-catenin signaling[J]. Cell, 2009, 139(2): 299-311.
[16] Nikopoulos K, Gilissen C, Hoischen A, et al. Next-generation sequencing of a 40 Mb linkage interval reveals TSPAN12 mutations in patients with familial exudative vitreoretinopathy[J]. Am J Hum Genet, 2010, 86(2): 240-7.
[17] Zhu X, Yang M, Zhao P, et al. Catenin α 1 mutations cause familial exudative vitreoretinopathy by overactivating Norrin/β-catenin signaling[J]. J Clin Invest, 2021, 131(6).
[18] Panagiotou E S, Sanjurjo Soriano C, Poulter J A, et al. Defects in the Cell Signaling Mediator β-Catenin Cause the Retinal Vascular Condition FEVR[J]. Am J Hum Genet, 2017, 100(6): 960-968.

[19] Liu Y, Yang M, Fan L, et al. Frameshift variants in the C-terminal of CTNNB1 cause familial exudative vitreoretinopathy by AXIN1-mediated ubiquitin-proteasome degradation condensation[J]. Int J Biol Macromol, 2023, 258(Pt 1): 128570.
[20] He Y, Yang M, Zhao R, et al. Novel truncating variants in CTNNB1 cause familial exudative vitreoretinopathy[J]. J Med Genet, 2023, 60(2): 174-182.
[21] Yang M, Li S, Huang L, et al. CTNND1 variants cause familial exudative vitreoretinopathy through the Wnt/cadherin axis[J]. JCI Insight, 2022, 7(14).
[22] Collin R W, Nikopoulos K, Dona M, et al. ZNF408 is mutated in familial exudative vitreoretinopathy and is crucial for the development of zebrafish retinal vasculature[J]. Proc Natl Acad Sci U S A, 2013, 110(24): 9856-61.
[23] Robitaille J M, Gillett R M, Leblanc M A, et al. Phenotypic overlap between familial exudative vitreoretinopathy and microcephaly, lymphedema, and chorioretinal dysplasia caused by KIF11 mutations[J]. JAMA Ophthalmol, 2014, 132(12): 1393-9.
[24] Khan K, Logan C V, Mckibbin M, et al. Next generation sequencing identifies mutations in Atonal homolog 7 (ATOH7) in families with global eye developmental defects[J]. Hum Mol Genet, 2012, 21(4): 776-83.
[25] Downey L M, Keen T J, Roberts E, et al. A new locus for autosomal dominant familial exudative vitreoretinopathy maps to chromosome 11p12-13[J]. Am J Hum Genet, 2001, 68(3): 778-81.
[26] Park H, Yamamoto H, Mohn L, et al. Integrin-linked kinase controls retinal angiogenesis and is linked to Wnt signaling and exudative vitreoretinopathy[J]. Nat Commun, 2019, 10(1): 5243.
[27] Zhang L, Zhang X, Xu H, et al. Exome sequencing revealed Notch ligand JAG1 as a novel candidate gene for familial exudative vitreoretinopathy[J]. Genet Med, 2020, 22(1): 77-84.
[28] Zhang S, Li X, Liu W, et al. Whole-Exome Sequencing Identified DLG1 as a Candidate Gene for Familial Exudative Vitreoretinopathy[J]. Genet Test Mol Biomarkers, 2021, 25(5): 309-316.
[29] Asano T, Oku K, Kondo H. Familial exudative vitreoretinopathy with TGFBR2 mutation without signs of Loeys-Dietz syndrome[J]. Ophthalmic Genet, 2021, 42(5): 637-640.
[30] Xu N, Cai Y, Li J, et al. An SNX31 variant underlies dominant familial exudative vitreoretinopathy-like pathogenesis[J]. JCI Insight, 2023, 8(10).
[31] Li S, Yang M, Zhao R, et al. Defective EMC1 drives abnormal retinal angiogenesis via Wnt/β-catenin signaling and may be associated with the pathogenesis of familial exudative vitreoretinopathy[J]. Genes Dis, 2023, 10(6): 2572-2585.
[32] Salvo J, Lyubasyuk V, Xu M, et al. Next-generation sequencing and novel variant determination in a cohort of 92 familial exudative vitreoretinopathy patients[J]. Invest Ophthalmol Vis Sci, 2015, 56(3): 1937-46.
[33] Kashani A H, Learned D, Nudleman E, et al. High prevalence of peripheral retinal vascular anomalies in family members of patients with familial exudative vitreoretinopathy[J]. Ophthalmology, 2014, 121(1): 262-268.

[34] Lindner A, Marbach F, Tschernitz S, et al. Calcyphosine-like (CAPSL) is regulated in Multiple Symmetric Lipomatosis and is involved in Adipogenesis[J]. Sci Rep, 2019, 9(1): 8444.
[35] Dang C V. A Time for MYC: Metabolism and Therapy[J]. Cold Spring Harb Symp Quant Biol, 2016, 81: 79-83.
[36] Beaulieu M E, Castillo F, Soucek L. Structural and Biophysical Insights into the Function of the Intrinsically Disordered Myc Oncoprotein[J]. Cells, 2020, 9(4).
[37] Carroll P A, Freie B W, Mathsyaraja H, et al. The MYC transcription factor network: balancing metabolism, proliferation and oncogenesis[J]. Front Med, 2018, 12(4): 412-425.
[38] Sander S, Calado D P, Srinivasan L, et al. Synergy between PI3K signaling and MYC in Burkitt lymphomagenesis[J]. Cancer Cell, 2012, 22(2): 167-79.
[39] De Alboran I M, O'hagan R C, Gärtner F, et al. Analysis of C-MYC function in normal cells via conditional gene-targeted mutation[J]. Immunity, 2001, 14(1): 45-55.
[40] Baudino T A, Mckay C, Pendeville-Samain H, et al. c-Myc is essential for vasculogenesis and angiogenesis during development and tumor progression[J]. Genes Dev, 2002, 16(19): 2530-43.
[41] Knies-Bamforth U E, Fox S B, Poulsom R, et al. c-Myc interacts with hypoxia to induce angiogenesis in vivo by a vascular endothelial growth factor-dependent mechanism[J]. Cancer Res, 2004, 64(18): 6563-70.
[42] Wilhelm K, Happel K, Eelen G, et al. FOXO1 couples metabolic activity and growth state in the vascular endothelium[J]. Nature, 2016, 529(7585): 216-20.
[43] Claxton S, Kostourou V, Jadeja S, et al. Efficient, inducible Cre-recombinase activation in vascular endothelium[J]. Genesis, 2008, 46(2): 74-80.
[44]Xia C H, Liu H, Cheung D, et al. A model for familial exudative vitreoretinopathy caused by LPR5 mutations[J]. Hum Mol Genet, 2008, 17(11): 1605-12.
[45] Rattner A, Williams J, Nathans J. Roles of HIFs and VEGF in angiogenesis in the retina and brain[J]. J Clin Invest, 2019, 129(9): 3807-3820.
[46] Saint-Geniez M, D'amore P A. Development and pathology of the hyaloid, choroidal and retinal vasculature[J]. Int J Dev Biol, 2004, 48(8-9): 1045-58.
[47] Ito M, Yoshioka M. Regression of the hyaloid vessels and pupillary membrane of the mouse[J]. Anat Embryol (Berl), 1999, 200(4): 403-11.
[48]Chen J, Stahl A, Krah N M, et al. Retinal expression of Wnt-pathway mediated genes in low-density lipoprotein receptor-related protein 5 (Lrp5) knockout mice[J]. PLoS One, 2012, 7(1): e30203.
[49] Fruttiger M. Development of the retinal vasculature[J]. Angiogenesis, 2007, 10(2): 77-88.
[50] Selvam S, Kumar T, Fruttiger M. Retinal vasculature development in health and disease[J]. Prog Retin Eye Res, 2018, 63: 1-19.
[51] Dorrell M I, Aguilar E, Friedlander M. Retinal vascular development is mediated by endothelial filopodia, a preexisting astrocytic template and specific R-cadherin adhesion[J]. Invest Ophthalmol Vis Sci, 2002, 43(11): 3500-10.
[52] Gerhardt H, Golding M, Fruttiger M, et al. VEGF guides angiogenic sprouting utilizing endothelial tip cell filopodia[J]. J Cell Biol, 2003, 161(6): 1163-77.

[53] Stenzel D, Lundkvist A, Sauvaget D, et al. Integrin-dependent and -independent functions of astrocytic fibronectin in retinal angiogenesis[J]. Development, 2011, 138(20): 4451-63.
[54] Luhmann U F, Lin J, Acar N, et al. Role of the Norrie disease pseudoglioma gene in sprouting angiogenesis during development of the retinal vasculature[J]. Invest Ophthalmol Vis Sci, 2005, 46(9): 3372-82.
[55] Hellström M, Gerhardt H, Kalén M, et al. Lack of pericytes leads to endothelial hyperplasia and abnormal vascular morphogenesis[J]. J Cell Biol, 2001, 153(3): 543-53.
[56] Knowland D, Arac A, Sekiguchi K J, et al. Stepwise recruitment of transcellular and paracellular pathways underlies blood-brain barrier breakdown in stroke[J]. Neuron, 2014, 82(3): 603-17.
[57] Liu Y, Senger D R. Matrix-specific activation of Src and Rho initiates capillary morphogenesis of endothelial cells[J]. Faseb j, 2004, 18(3): 457-68.
[58] Fujiwara H, Gu J, Sekiguchi K. Rac regulates integrin-mediated endothelial cell adhesion and migration on laminin-8[J]. Exp Cell Res, 2004, 292(1): 67-77.
[59] Fischer R S, Gardel M, Ma X, et al. Local cortical tension by myosin II guides 3D endothelial cell branching[J]. Curr Biol, 2009, 19(3): 260-5.
[60] Santos-Oliveira P, Correia A, Rodrigues T, et al. The Force at the Tip--Modelling Tension and Proliferation in Sprouting Angiogenesis[J]. PLoS Comput Biol, 2015, 11(8): e1004436.
[61] Birdsey G M, Shah A V, Dufton N, et al. The endothelial transcription factor ERG promotes vascular stability and growth through Wnt/β-catenin signaling[J]. Dev Cell, 2015, 32(1): 82-96.
[62] Coxam B, Sabine A, Bower N I, et al. Pkd1 regulates lymphatic vascular morphogenesis during development[J]. Cell Rep, 2014, 7(3): 623-33.
[63] Kim Y H, Choi J, Yang M J, et al. A MST1-FOXO1 cascade establishes endothelial tip cell polarity and facilitates sprouting angiogenesis[J]. Nat Commun, 2019, 10(1): 838.
[64] Carvalho J R, Fortunato I C, Fonseca C G, et al. Non-canonical Wnt signaling regulates junctional mechanocoupling during angiogenic collective cell migration[J]. Elife, 2019, 8.
[65] Franco C A, Jones M L, Bernabeu M O, et al. Correction: dynamic endothelial cell rearrangements drive developmental vessel regression[J]. PLoS Biol, 2015, 13(5): e1002163.
[66] Kwon H B, Wang S, Helker C S, et al. In vivo modulation of endothelial polarization by Apelin receptor signalling[J]. Nat Commun, 2016, 7: 11805.
[67] Potente M, Gerhardt H, Carmeliet P. Basic and therapeutic aspects of angiogenesis[J]. Cell, 2011, 146(6): 873-87.
[68] De Smet F, Segura I, De Bock K, et al. Mechanisms of vessel branching: filopodia on endothelial tip cells lead the way[J]. Arterioscler Thromb Vasc Biol, 2009, 29(5): 639-49.
[69] Kurz H, Gärtner T, Eggli P S, et al. First blood vessels in the avian neural tube are formed by a combination of dorsal angioblast immigration and ventral sprouting

of endothelial cells[J]. Dev Biol, 1996, 173(1): 133-47.
[70] Marin-Padilla M. Early vascularization of the embryonic cerebral cortex: Golgi and electron microscopic studies[J]. J Comp Neurol, 1985, 241(2): 237-49.
[71] Ruhrberg C, Gerhardt H, Golding M, et al. Spatially restricted patterning cues provided by heparin-binding VEGF-A control blood vessel branching morphogenesis[J]. Genes Dev, 2002, 16(20): 2684-98.
[72] Fraccaroli A, Pitter B, Taha A A, et al. Endothelial alpha-parvin controls integrity of developing vasculature and is required for maintenance of cell-cell junctions[J]. Circ Res, 2015, 117(1): 29-40.
[73] Hall A. Rho GTPases and the control of cell behaviour[J]. Biochem Soc Trans, 2005, 33(Pt 5): 891-5.
[74] Lourenco C, Resetca D, Redel C, et al. MYC protein interactors in gene transcription and cancer[J]. Nat Rev Cancer, 2021, 21(9): 579-591.
[75] Andrade J, Shi C, Costa A S H, et al. Control of endothelial quiescence by FOXO-regulated metabolites[J]. Nat Cell Biol, 2021, 23(4): 413-423.
[76] Dang C V. MYC, metabolism, cell growth, and tumorigenesis[J]. Cold Spring Harb Perspect Med, 2013, 3(8).
[77] Adhikary S, Eilers M. Transcriptional regulation and transformation by Myc proteins[J]. Nat Rev Mol Cell Biol, 2005, 6(8): 635-45.
[78] Dang C V. MYC on the path to cancer[J]. Cell, 2012, 149(1): 22-35.
[79] Stine Z E, Walton Z E, Altman B J, et al. MYC, Metabolism, and Cancer[J]. Cancer Discov, 2015, 5(10): 1024-39.
[80] Martowicz A, Trusohamn M, Jensen N, et al. Endothelial β-Catenin Signaling Supports Postnatal Brain and Retinal Angiogenesis by Promoting Sprouting, Tip Cell Formation, and VEGFR (Vascular Endothelial Growth Factor Receptor) 2 Expression[J]. Arterioscler Thromb Vasc Biol, 2019, 39(11): 2273-2288.
[81] Green S, Hoover T, Doss D, et al. WNT-activated, MYC-amplified medulloblastoma displaying intratumoural heterogeneity[J]. Neuropathol Appl Neurobiol, 2023: e12945.
[82] Rennoll S, Yochum G. Regulation of MYC gene expression by aberrant Wnt/β-catenin signaling in colorectal cancer[J]. World J Biol Chem, 2015, 6(4): 290-300.
[83] Cairo S, Armengol C, Buendia M A. Activation of Wnt and Myc signaling in hepatoblastoma[J]. Front Biosci (Elite Ed), 2012, 4(1): 480-6.
[84] Barry D M, Xu K, Meadows S M, et al. Cdc42 is required for cytoskeletal support of endothelial cell adhesion during blood vessel formation in mice[J]. Development, 2015, 142(17): 3058-70.
[85] Zihni C, Mills C, Matter K, et al. Tight junctions: from simple barriers to multifunctional molecular gates[J]. Nat Rev Mol Cell Biol, 2016, 17(9): 564-80.
[86] Liu W, Jiang X, Li X, et al. LMBR1L regulates the proliferation and migration of endothelial cells through Norrin/β-catenin signaling[J]. J Cell Sci, 2022, 135(6).
[87] Yang Y, Liu W, Sun K, et al. Tmem30a deficiency leads to retinal rod bipolar cell degeneration[J]. J Neurochem, 2019, 148(3): 400-412.
[88] Zhang S, Liu W, Yang Y, et al. TMEM30A deficiency in endothelial cells impairs

cell proliferation and angiogenesis[J]. J Cell Sci, 2019, 132(7).

Figures and Figure legends

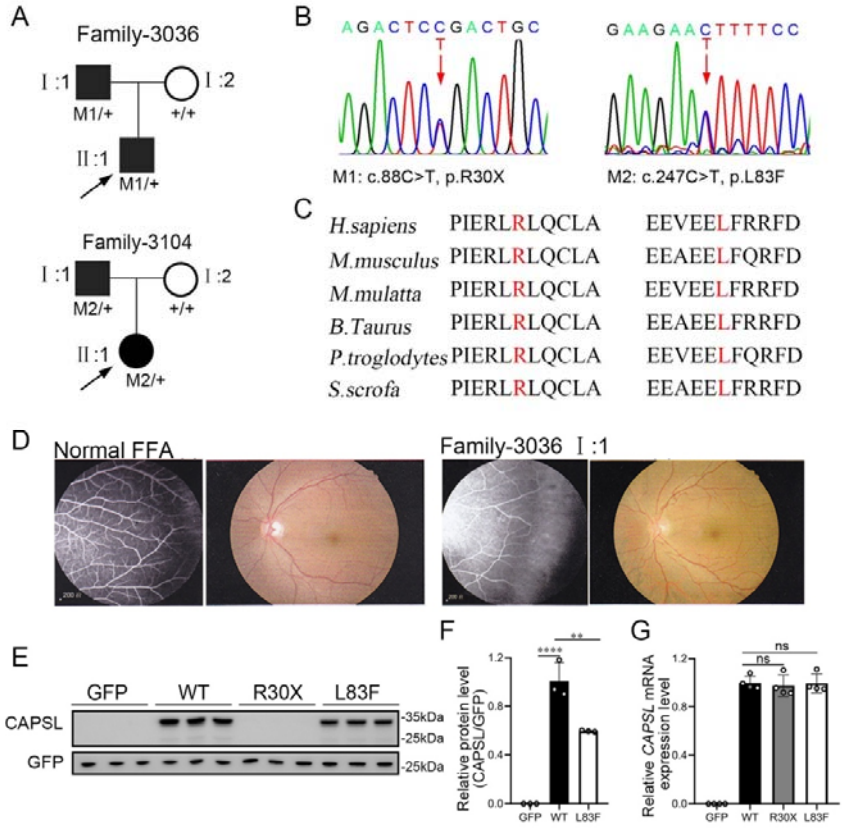

Figure 1. *CAPSL* point mutations in two families with familial exudative vitreoretinopathy (FEVR).

(A-B) FEVR pedigrees (patients are denoted with black symbols) and Sanger sequencing of two heterozygous mutations identified in two families. Black arrows indicate the proband of each family and red arrows indicate the changed nucleotides. **(C)** Alignment of amino sequences surrounding the *CAPSL* variants in different species and all mutated sites are highly conserved. Altered amino acid residues are

highlighted in red. **(D)** Fundus fluorescein angiography (FFA) (left panel) and fundus photography (right panel) of a normal individual and FEVR-affected patient (I:1) in family 3036. **(E-G)** Western blot **(E-F)** and RT-qPCR analysis **(G)** of *CAPSL* expression of WT and mutant plasmids. An empty vector with GFP tag was used as a negative control. GFP was used as an internal reference. Error bars indicate the SD. **P < 0.01, ****P < 0.0001, ns: no significance, by Student's t test (n = 3).

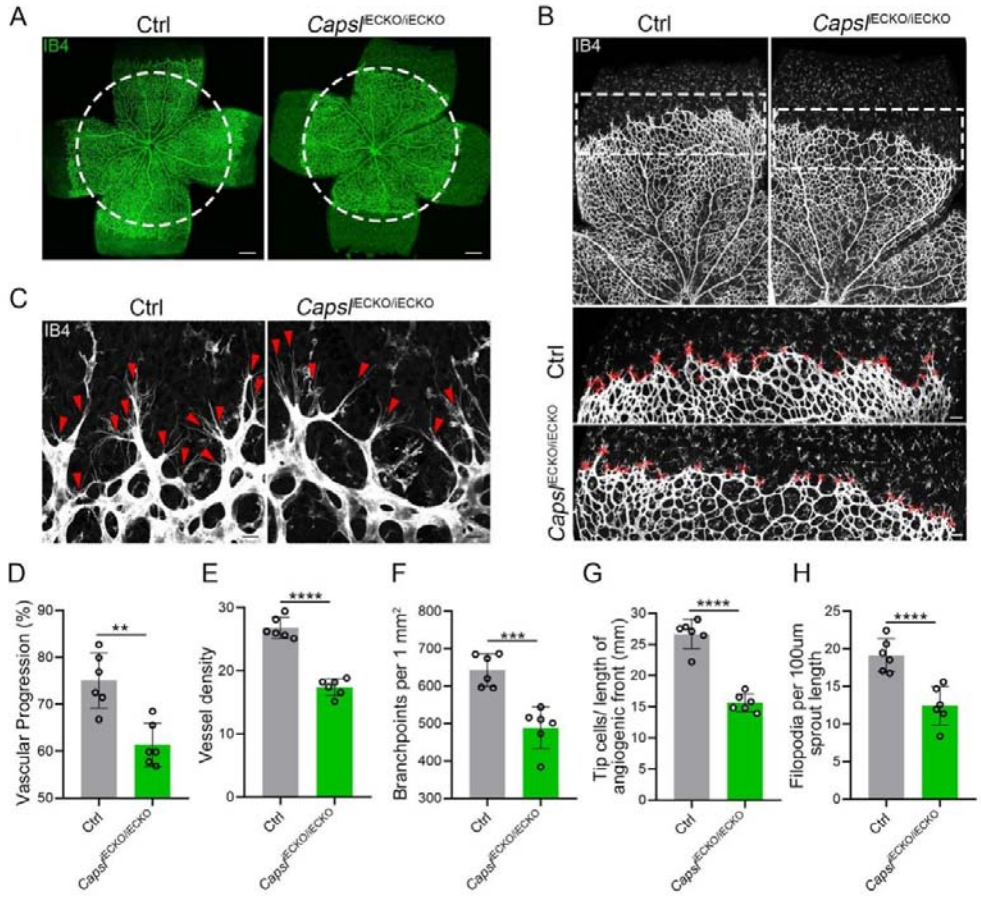

Figure 2. EC-specific inactivation of *Capsl* impairs retina angiogenesis.

(A) Flat-mounted retinas obtained from P5 Ctrl and littermate *Capsl*$^{iECKO/iECKO}$ mice were stained with Isolectin-B4 (IB4) to visualize blood vessel. Dashed circle mark the edge of the developing retina vessel in *Capsl*$^{iECKO/iECKO}$ mice. Scale bar: 250 μm. **(B)** Low magnification images (top panels) and high magnification images (bottom panels) in boxed areas of IB4-stained angiogenic front of Ctrl and *Capsl*$^{iECKO/iECKO}$ mice, respectively. Red cross mark tip cells at the angiogenic growth front. Scale bar: 100 μm (top panels), 25 μm (bottom panels). **(C)** High magnification images of

filopodia-extending cells at the edge of retinal angiogenic growth front from Ctrl and *Capsl*$^{iECKO/iECKO}$ mice. Red arrowheads indicate the sprouts at the angiogenic growth front. **(D-H)** Quantification of retinal vascular development parameters, including vascular progression, vessel density, branchpoints, number of tip cells, and number of filopodia. Error bars indicate the SD. **P < 0.01, ***P < 0.001, ****P < 0.0001, by Student's t test (n = 6).

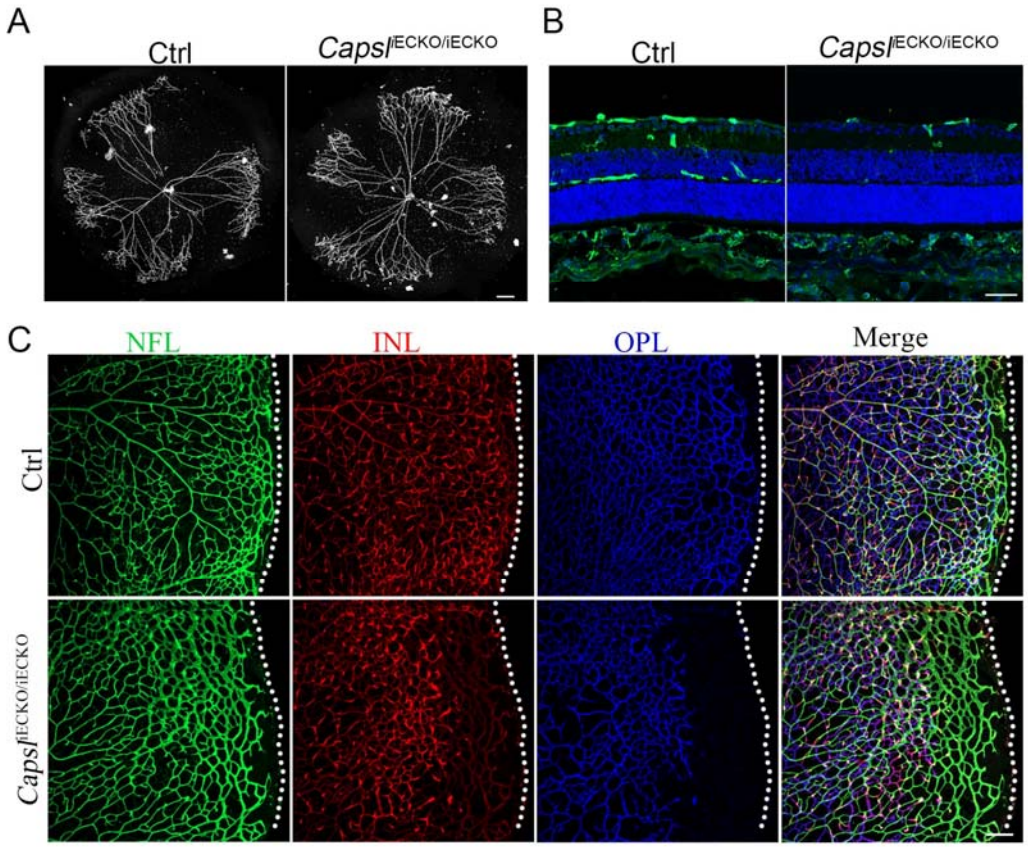

Figure 3. Loss of *Capsl* results in delayed hyaloid regression and deep retinal blood vessel growth.

(A) Hyaloid vessels stained with DAPI in the eyes of Ctrl and *Capsl*$^{iECKO/iECKO}$ mice at P10. Scale bar: 250 μm. **(B)** Retina sections from P10 Ctrl and *Capsl*$^{iECKO/iECKO}$ mice were costained with IB4 (greed) and DAPI (blue). Scale bar: 100 μm. **(C)** Flat-mounted retains stained with IB4 at P14 Ctrl and *Capsl*$^{iECKO/iECKO}$ mice. Optical sections of z-stacked confocal images were divided to represent the nerve fiber layer (NFL), inner plexiform layer (INL), and outer plexiform layer (ONL). Dashed lines

mark the edge of the developing retina. Scale bar: 100 μm

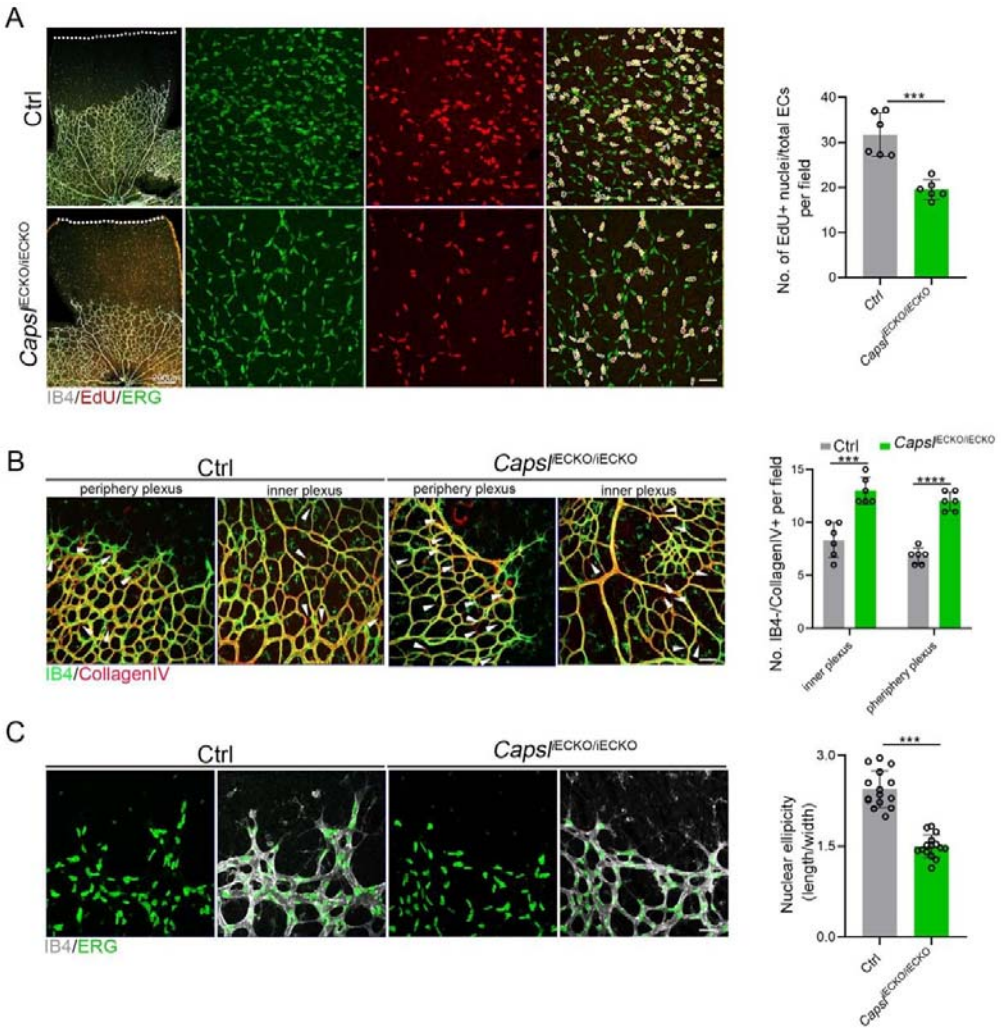

Figure 4. Deletion of *Capsl* impairs EC proliferation and migration.

(A) Retina endothelial cell proliferation of Ctrl and *Capsl*$^{iECKO/iECKO}$ mice at the vitreal surface was measured with EdU and ERG labeling at P5. Images captured at higher magnification are shown at right. Dashed lines mark the edge of the developing retina, and dashed circles represent both EdU+ and ERG+ cells. EC proliferation ability was

measured by the ration of EdU+ and ERG+ cells per vascular area. Scale bar: 200 μm and 50 μm (enlarged insets). Error bars indicate the SD. ***P < 0.001, by Student's t test (n = 6). **(B)** Representative images of retinal vessels at the periphery plexus and inner plexus of Ctrl and *Capsl*$^{iECKO/iECKO}$ mice at P5 costained with IB4 (green) and Collagen IV (red). Arrowhead point to empty Collagen IV sleeves. And quantification of ratio of Collagen IV positive vessel segments to IB4 labeling-negative vessel segments. Scale bar: 50 μm. Error bars indicate the SD. ***P < 0.001, ****P < 0.0001, by Student's t test (n = 6). **(C)** Magnified images of IB4+ vessels and ERG+ nuclei of ECs at angiogenic front of Ctrl and *Capsl*$^{iECKO/iECKO}$ mice at P5. Quantification of tip cell nuclear ellipicity at the angiogenic growth front. Scale bar: 50 μm. Error bars indicate the SD. ***P < 0.001, by Student's t test (n = 14).

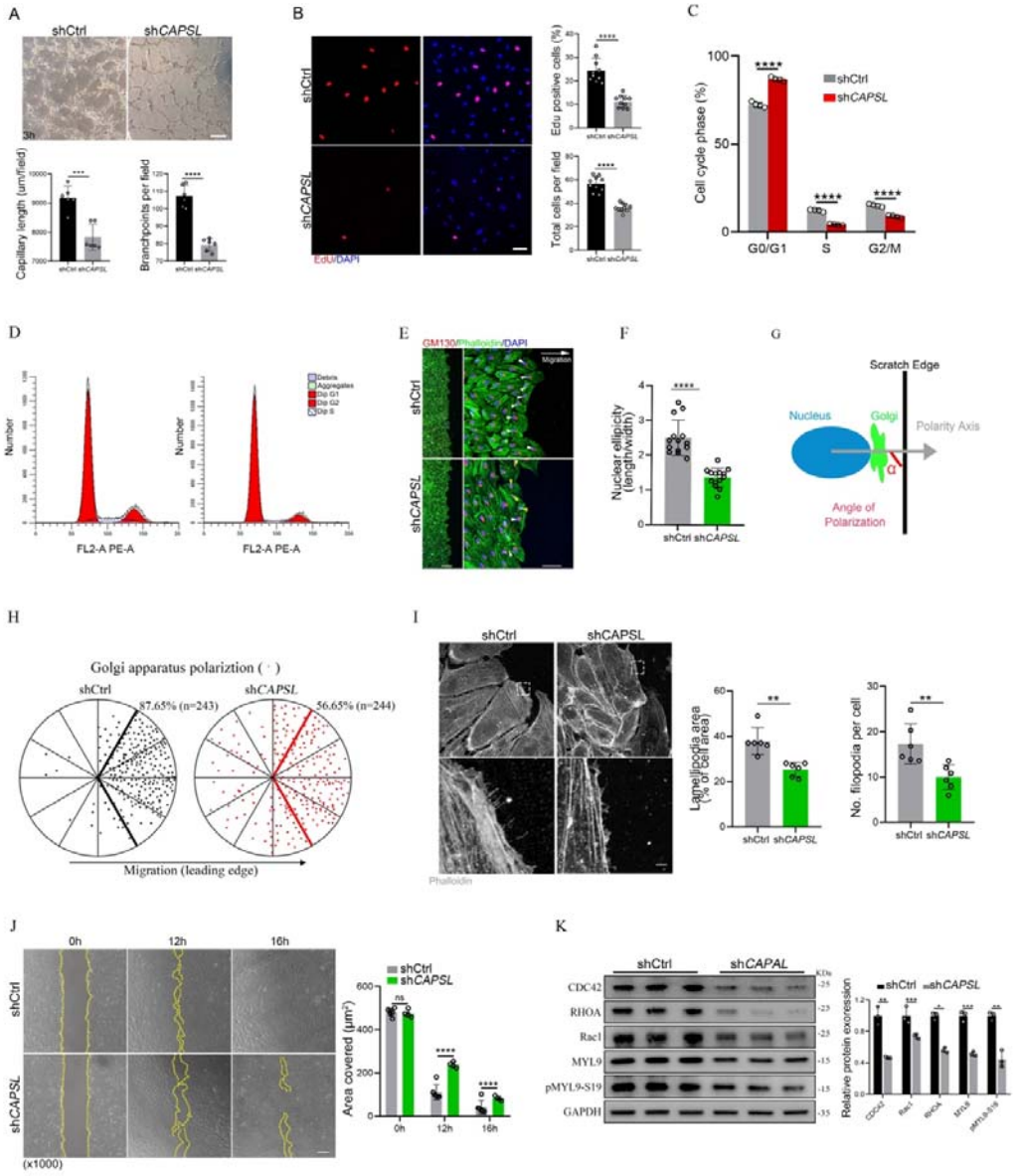

Figure 5. Depletion of *CAPSL* in HRECs compromises *in vitro* EC proliferation and migration.

(A) Representative images of *in vitro* tube formation after transfection of HRECs with shRNA. Scale bar: 200 μm. Error bars indicate the SD. ***P < 0.001, ****P < 0.0001, by Student's t test (n=6). **(B)** Incorporation of EdU in shRNA transfected HRECs. Representative confocal images and quantification of proliferating HRECs both in number per field and proportion of EdU-positive cells. Scale bar: 50 μm. Error bars indicate the SD. ****P < 0.0001, by Student's t test (n=10). **(C-D)** Cell cycle analysis of shCtrl-ECs and sh*CAPSL*-ECs by flow cytometry. Error bars indicate the SD. ****P < 0.0001, by Student's t test (n=4). **(E)** Representative

images of phalloidin actin cytoskeleton (green) and GM130 (red) showing polarity angles of shCtrl-ECs and sh*CAPSL*-ECs at the edge of scratch wound. The arrow points toward the wound. Colored arrowheads represent different migration state. Scale bar: 200 μm (left panel) 50 μm (right panel). **(F)** Quantification of nuclear ellipticity of HRECs at the margin of wound scratch. Error bars indicate the SD. ****P < 0.0001, by Student's t test (n = 14). **(G)** Schematic pictures showing the define of polarity axis of each cell. Polarity axis was measured with the angle (α) between the scratch edge and the vector drawn from the center of nucleus to the center of the Golgi apparatus. **(H)** Polar plots showing Golgi apparatus polarization. The bold lines represent 120° region centered on the vector, which is perpendicular to the wound scratch. The dots represent the angle (α) of each cell and the numbers indicate the frequency of dots within the 120° region of the bold line of shCtrl-ECs (n=243) and sh*CAPSL*-ECs (n=244). **(I)** Images of phalloidin-stained actin cytoskeleton and comparisons of indicated parameters in shCtrl-ECs and sh*CAPSL*-ECs at the edge of scratch wound. The dashed boxed region is shown at higher magnification at the bottom panel. Scale bar: 50 μm (top panels), 25 μm (bottom panels). **(J)** Representative images of wound scratch assay at 0h, 12h, and 16h after wound was made. And the quantification of covered area at different time point. The dashed line indicates the gap of the wound after wound scratch at different time point. Scale bar: 200 μm. Error bars indicate the SD. ****P < 0.0001, ns : no significance, by Student's t test (n = 4). **(K)** Immunoblot and quantification analysis of expression of small GTPase proteins and a key regulator of contractile force MYL9 in shCtrl-ECs and sh*CAPSL*-ECs. Error bars indicate the SD. *P < 0.05, **P < 0.01, ***P < 0.001, by Student's t test (n = 3).

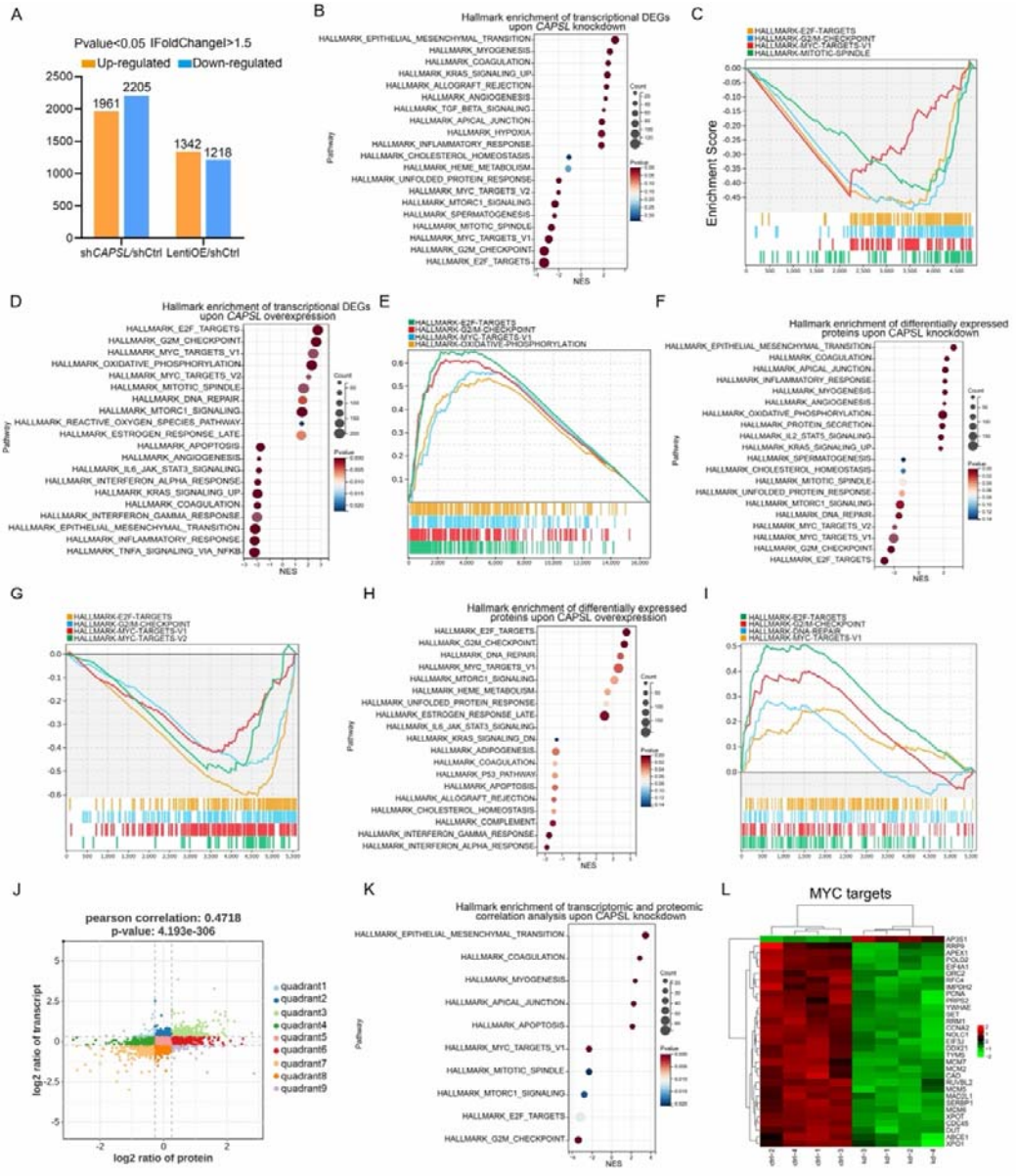

Figure 6. *CAPSL* suppresses MYC signaling axis.

(A) Differential gene expression information of sh*CAPSL*-ECs versus shCtrl-ECs group and LentiOE-ECs versus shCtrl-ECs group. **(B-E)** Gene set enrichment analysis (GSEA) analysis on the RNA sequencing data of HRECs. Top 10 ranked up or down regulated signaling axis were listed **(B)** and top 4 down-regulated gene sets were listed **(C)** in comparison of shCtrl-ECs versus sh*CAPSL*-ECs. Top 10 ranked up or down regulated signaling axis were listed **(D)** and top 4 up-regulated gene sets were

listed **(E)** in comparison of LentiOE-ECs versus shCtrl-ECs. **(F-I)** Gene set enrichment analysis (GSEA) analysis on the proteomic profiling data of HRECs. Top 10 ranked up or down regulated signaling axis were listed **(F)** and top 4 down-regulated gene sets were listed **(G)** in comparison of shCtrl-ECs versus sh*CAPSL*-ECs. Top 10 ranked up or down regulated signaling axis were listed **(H)** and top 4 up-regulated gene sets were listed **(I)** in comparison of LentiOE-ECs versus shCtrl-ECs. **(J)** Correlated RNAs and proteins enriched in nine quadrants of shCtrl-ECs versus sh*CAPSL*-ECs. **(K)** Gene set enrichment analysis (GSEA) analysis on the genes/proteins in quadrants 3 and 7, and top 5 ranked up or down regulated signaling axis were listed. **(L)** Clustered heat map of the expression fold changes of several MYC signature genes of in both RNA profiling and proteomic profiling of shCtrl-ECs and sh*CAPSL*-ECs.

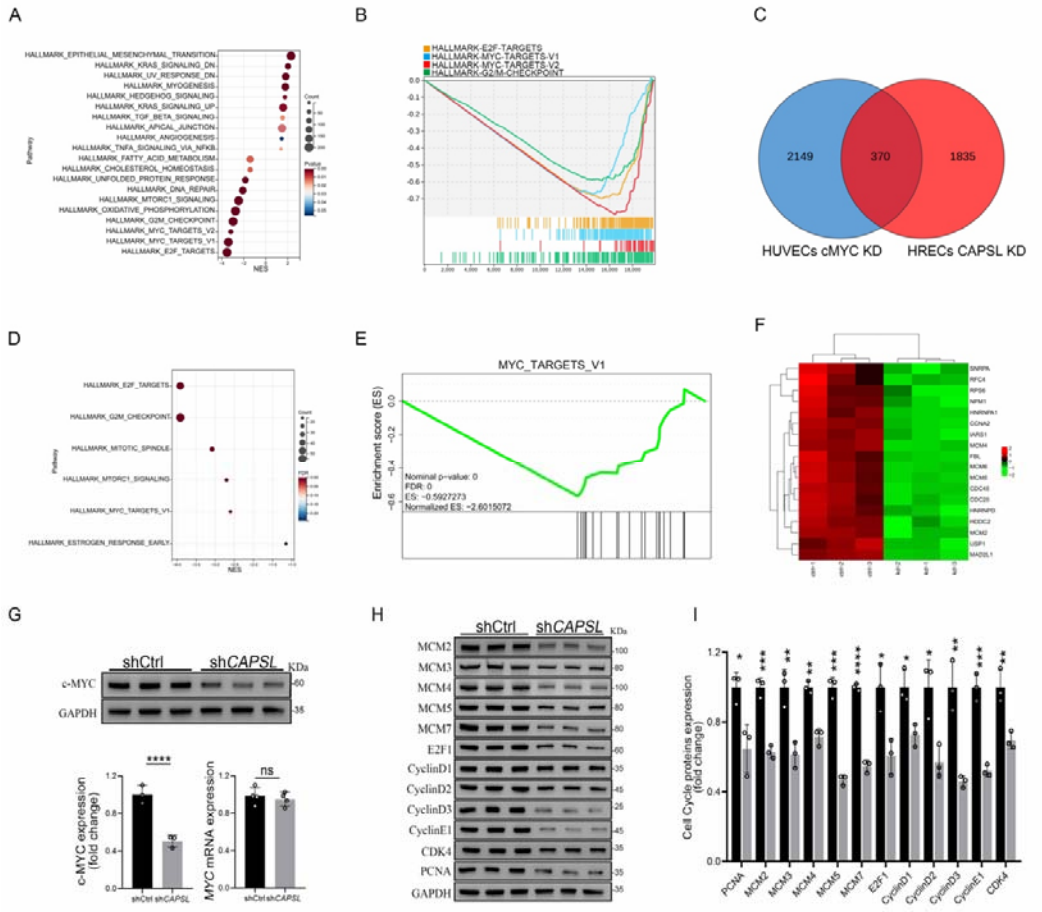

Figure 7. Loss of *CAPSL* led to similar transcriptional regulatory patterns to the loss of *c-MYC* in HUVECs.

(A-B) Gene set enrichment analysis (GSEA) analysis on the RNA sequencing data in comparison of shCtrl-HUVECs versus sh*c-MYC*-HUVECs. Top 10 ranked up or down regulated signaling axis were listed **(A)** and top 4 down-regulated gene sets were listed **(B). (C)** Venn diagram analysis of down-regulated genes in *CAPSL*-depleted HRECs and *c-MYC*-depleted HUVECs. **(D-E)** Gene set enrichment analysis (GSEA) analysis on the shared down-regulated genes in *CAPSL*-depleted HRECs and *c-MYC*-depleted HUVECs. **(F)** Heatmap of MYC signature genes of shared genes based on Venn analysis. **(G)** c-MYC expression level in shCtrl-ECs and sh*CAPSL*-ECs was quantified by western blot and RT-qPCR. Error bars indicate the SD. ****P < 0.0001, ns: no significance by Student's t test (n = 3). **(H)** Western blot analysis of expression of MYC targets. **(I)** Quantification analysis of MYC targets.

Error bars indicate the SD. *P < 0.05, **P < 0.01, ***P < 0.001, ****P < 0.0001, by Student's t test (n = 3)